18.01% Efficiency organic solar cell and 2.53% light utilization efficiency semitransparent organic solar cell enabled by optimizing PM6:Y6 active layer morphology

Kuibao Yu[1,3], Wei Song[1,2], Jinfeng Ge[1,2], Kanghui Zheng[1,3], Lin Xie[1], Zhenyu Chen[1,2], Yi Qiu[1,2], Ling Hong[1*], Cuirong Liu[3*] & Ziyi Ge[1,2*]

[1]*Zhejiang Provincial Engineering Research Center of Energy Optoelectronic Materials and Devices, Ningbo Institute of Materials Technology & Engineering, Chinese Academy of Sciences, Ningbo 315201, China;*
[2]*Center of Materials Science and Optoelectronics Engineering University of Chinese Academy of Sciences, Beijing 100049, China;*
[3]*College of Materials Science and Engineering, Taiyuan University of Science and Technology, Taiyuan 030024, China*

Optimizing the photoactive layer morphology is a simple, promising way to improve the power conversion efficiencies (PCEs) of organic solar cells (OSCs). Here, we compared different post-processing treatments on PM6:Y6 blend films and relevant effects on device performances, including as-cast, thermal annealing and solvent annealing. This solvent annealing processes can effectively improve the vertical distribution and aggregation of polymer donors and small molecule acceptors, then optimize the active layer film morphology, ultimately elevating PCE. Thus, one of champion efficiencies of 18.01% was achieved based on the PM6:Y6 binary OSCs. In addition, a relatively high light utilization efficiency (2.53%) was achieved when a transparent electrode made of Cu (1 nm) and Ag (15 nm) was utilized to fabricate a semitransparent OSC with a remarkable PCE of 13.07% and 19.33% average visible-light transmittance. These results demonstrated that carefully optimizing morphology of active layer is conducive to achieving a high-performance OSC.

organic solar cells, solvent vapor annealing, morphology optimization, light utilization efficiency

1 Introduction

In recent years, organic solar cells (OSCs) have attracted widespread attention, owing to their advantages of light-weight, flexibility, simple preparation process, semi-transparency, and compatibility with large-area manufacturing [1–6]. Benefiting from the development of photovoltaic materials design, optimized morphology, and device engineering, over 19% power conversion efficiency (PCE) of OSCs has been achieved [7–10]. The morphology is a bridge that connects materials properties and device performances. Its microstructure achieves well-ordered crystalline domains as well as favorable charge transport properties, and these results can further improve device performances [11–14]. To date, several strategies to effectively control the microstructure of blends have been certified, covering thermal annealing (TA), solvent vapor annealing (SVA), and additives, *etc*. [13]. These morphological control methods are favorable for achieving excellent interpenetration of networks with nanoscale domain sizes as well as suitable interfacial region, which positively affects

---

the optics and electronics of blends [15–18].

In the aspect of morphology control, TA and SVA, as the most universal post-process in bulk-heterojunction (BHJ) systems, including fullerene-based and non-fullerene-based systems, can effectively improve the photovoltaic performance of the devices [19–21]. Toney *et al.* [22] reported the 7.5% efficiency organic solar cell with SVA-treated P3HT:PC$_{71}$BM. Liu's group [18] adopted TA-treatment to obtain 16.88% efficiency *via* fine-tuning film morphology based on PM6:Y6. Loi's group [15] employed SVA to induce phase separation of the active layer TPD-3F:IT-4F and increase its crystallinity, resulting in increased photogenerated current with more efficient exciton dissociation and charge collection, which obtained an excellent 13.8% PCE. Ade *et al.* [23] presented the superior effectiveness of SVA based on polymer. The SVA treatment remarkably increases the coherence length of the π-π stacking of D18 as well as increases the crystallinity of both D18 and NFAs. In general, both TA and SVA are applied to promote molecular crystallization, resulting in improved phase separation, but among different implementation process. As for the TA-treatment, the film is evaporated by heating for several minutes to rearrange the shape and then adjust the self-aggregation and crystallization [16,24,25]. During SVA, solvent molecules diffuse into the active layer and increase the mobility of molecules within the active layer, leading to reorganization and efficient control of the morphology of the BHJ blend [13]. Hence, SVA is an especially helpful and efficient method for finely tuning film morphology of OSCs, as it can promote the aggregation of both donor and acceptor molecules in the mixing regions [26–29]. Then, an increased length scale of phase separation and improved domain purity can be achieved.

In this work, we systematically investigated the performance differences of OSCs based on polymer donor PM6 and NFA Y6 of active layers with CS$_2$-SVA, TA, and as-cast conditions. Benefited from the improved molecular crystallinity and phase separation, in comparison with TA-and as-cast, the CS$_2$-optimized devices presented more favorable phase separation. Therefore, the CS$_2$-optimized devices exhibited higher exciton dissociation, less charge combination, higher and more balanced hole and electron mobility. These results eventually drive short-circuit current density (J_{SC}) and fill factor (FF), leading to better PCEs. As a result, high PCE of 18.01% with a substantially increased J_{SC} of 27.46 mA cm^{-2} and FF of 78.19% was acquired, which is significantly higher than that of OSCs based on as-cast and TA-processed PM6:Y6 active layer. Impressively, the J_{SC} for PM6:Y6 binary OSC increased to over 27 mA cm^{-2}, an increase which is ascribed to the generation of enhanced photon collection in the near-infrared range (NIR). The significance of semitransparent OSCs is achieved for practical application. The high-performance semitransparent OSCs are required to capture more photons in the infrared

range but selectively transmit in the visible range [30–32]. Therefore, we used Cu (1 nm) and Ag (15 nm) as top electrodes to fabricate high-performance semitransparent devices among the CS$_2$-based condition with PCE of 13.07% and AVT of 19.33%.

2   Result and discussion

The classic polymer PM6 and small molecule Y6 were chosen as a donor and a acceptor, respectively [33]. Corresponding molecular structures and energy levels are presented in Figure 1a and Figure S1b (Supporting Information online). The device structure (indium tin oxide(ITO)/poly (3,4-ethylenedioxythiophene):poly(styrenesulfonate) (PED-OT:PSS)/poly[4,8-bis(5-(2-ethylhexyl)4-fluorothiophen-2-yl) benzo[1,2-b:4,5-b′]-dithiophene-*alt*-1,3-bis(thiophen-2-yl)-5,7-bis(2-ethylhexyl)benzo-[1,2-c:4,5-c′]-dithiophene-4,8-dione]   (PM6):2,2'-((2Z,2'Z)-((12,13-bis(2ethylhexyl)-3,9-diundecyl-12,13-dihydro-[1,2,5] thiadiazolo[3,4-e]thieno[2'',3'':4',5']thieno[2',3':4,5] pyrrolo[3,2-g]thieno[2',3':4,5] thieno[3,2-b]indole-2,10-diyl)bis(methanylylidene))bis(5,6-difluoro-3-oxo-2,3-dihydro-1H-indene-2,1-diylidene))   dimalononitrile (Y6)/aliphatic amine-functionalized perylenediimide (PDINN)/Ag) and the molecular structures of the interface materials are shown in Figure S1a and Figure S2. The detailed procedures of device fabrication are described in the Supporting Information online. The corresponding current density-voltage (*J-V*) curves and device parameters of OSCs are shown in Figure 1b and Table 1. The devices based on as-cast PM6:Y6 active layer produce a high PCE of 16.57% with J_{SC} of 25.74 mA cm^{-2} and FF of 75.11%, which is remarkable for OSCs under as-cast processing. J_{SC} and FF of devices with TA-treated active layer are slightly improved, resulting in a PCE of 17.02%. Due to the increased intermolecular interactions between the donor and the acceptor, J_{SC} and FF of CS$_2$-treated active layer-based devices increased to 27.46 mA cm^{-2} and 78.19%, respectively, and a high PCE of 18.01% was obtained. Notably, the PCE of 18.01% presents the highest-performing binary OSCs based on PM6:Y6 system reported to date [34,35]. As demonstrated in Figure 1b, the external quantum efficiencies (EQE) were characterized to better analyze the J_{SC} values of OSCs with different treatment processes. It could be seen that CS$_2$-treated devices present a broader EQE response spectrum than that of TA-treated device, which is consistent with the measured absorption results, also illustrating the higher J_{SC}. From Table 1, the values of the calculated J_{SC} extracted from EQE spectrum are consistent well with the current densities from *J-V* curves (within 5% error range). The difference between the CS$_2$, TA, and as-cast treatment OSCs, defined as the EQE spectral discrepancy (ΔEQE) is illustrated in Figure S3a. It was found that the CS$_2$-treated devices' positive
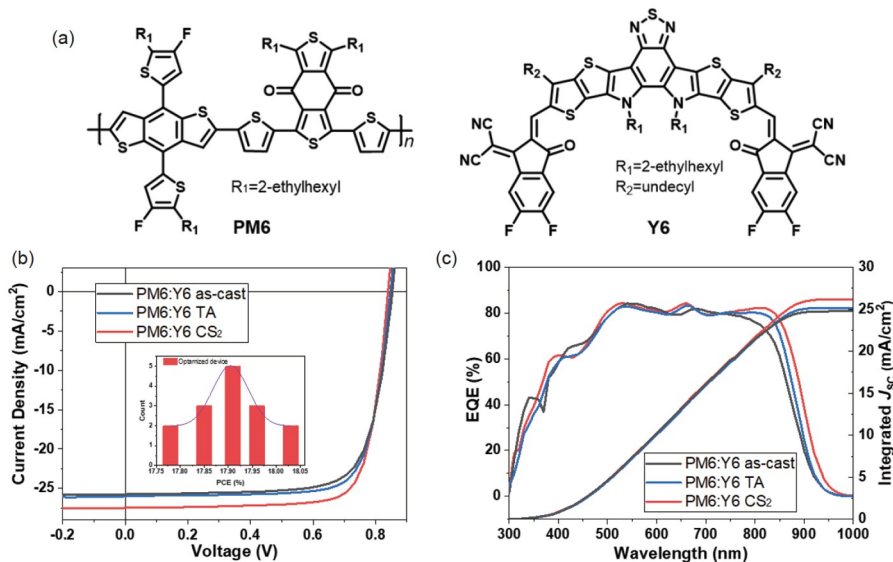
Figure 1 (a) Molecule structures; (b) the *J-V* curves for optimized devices with various treatments and efficiency statistical histogram for 15 CS_2-treated devices; (c) EQE spectrum devices based on PM6:Y6 active layer with various treatments (color online).

Table 1 Photovoltaic parameters of OSCs based on different processing PM6:Y6 system

	V_{OC} (V)	J_{SC} (mA cm^{-2})	$J_{calc.}$ [a] (mA cm^{-2})	FF (%)	PCE (Ave±Dev.) [b] (%)
As-cast	0.857	25.74	24.76	75.11	16.57 (16.38±0.10)
TA	0.849	25.99	25.19	77.17	17.02 (16.91±0.08)
CS_2	0.839	27.46	26.19	78.19	18.01 (17.90±0.07)

a) The values of J_{SC} were calculated from EQE spectrum; b) average and deviation of 15 device samples.

ΔEQE curve covers from 470–540 and 730–1,000 nm range, comparatively better than that of as-cast treated devices. Impressively, compared with TA-treated devices, the positive ΔEQE curve covers from 300–1,000 nm, and furthermore, has increased significantly at 800–1,000 nm range. This result illustrated the higher J_{SC} for CS_2-treated devices, which is ascribed to the enhanced spectral utilization and optimized phase separation after CS_2 process [36,37]. Figure S3b presents absorption spectra of PM6:Y6 blend films based on different treatment processing. When treated with CS_2-processing, the spectra of blend films were broadened in comparison with both the as-cast and TA-treatment films. These results would be derived from the induced crystallization of PM6 and Y6 [21,38], accompanying the improvement of film morphology. Such a broad absorption is beneficial to OSCs to absorb more sunlight, producing a larger photocurrent.

For deeper insight of the molecular packing and texture with different treated devices, grazing-incidence wide-angle X-ray scattering (GIWAXS) was conducted to characterize and analyze the neat and blend films, as shown in Figure 2a, b, and the related parameters are listed in Table S1 (Supporting Information online). From analysis, it is obvious that the neat PM6 films exhibit the same stacking distance of 3.778 Å (Q_Z=1.663 Å^{-1}) with CS_2-and TA-treated ones, and

the stacking distance is lower than that of 3.874 Å (Q_Z=1.622 Å^{-1}) from as-cast treatment. Similarly, the original Y6 films with as-cast and TA-treatment produce the same stacking distance of 3.682 Å (Q_Z=1.706 Å^{-1}), whereas the CS_2-treatment dispatches a shorter distance of 3.592 Å (Q_Z=1.749 Å^{-1}). These results imply that Y6 is much sensitive to CS_2-treatment, producing more ordered stacking. By contrast, all the blend films show a clear diffraction peak and the same π-π stacking along the out of plane (OOP) direction, indicating a dominant face-on orientation, which is beneficial to improving charge transfer. These (010) diffraction peaks enable us to quantitatively extract the π-π stacking crystal coherence lengths (CCL) of the neat and blend films using the Scherrer equation. The CS_2-treated PM6 film showed the highest values of CCL (21.56 Å) in comparison with as-cast (20.431 Å) and TA- (20.943 Å), respectively. Comparing TA- and as-cast treated Y6 films, we see CS_2-treated Y6 neat film exhibited the higher CCL of 23.562 Å. Consequently, the blend film based on CS_2-annealing produced higher CCL of 22.383 Å, in contrast to either TA- (22.05 Å) or as-cast (21.482 Å), which could attribute to CS_2-annealing improved donor and acceptor crystallization. The increased CCL values with the CS_2-treated blend films mean higher molecular crystallinity in domains, which could promote intermolecular charge transport and reduce charge re-
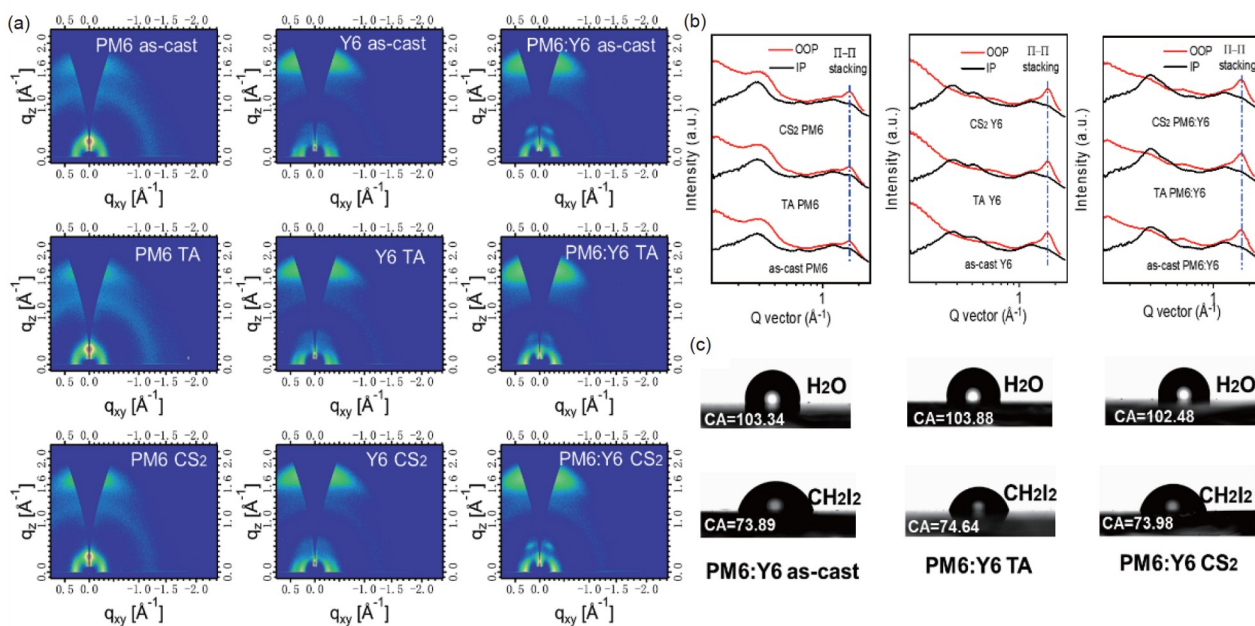
Figure 2   (a) GIWAXS patterns and (b) corresponding GIWAXS intensity profiles along the out-of-plane and in-plane directions; (c) contact angle images of PM6:Y6 blend films with and without processing (color online).

combination, thereby leading to the significantly improved J_{SC} and FF of the device [39,40].

To clarify the impact of the morphology of the PM6:Y6 blend, we investigated the surface tension (γ_s) of the blend films *via* measuring the contact angle. Contact angle measurements of water and CH_2I_2 were performed on pure films and their blends under different processing, as provided in Figures S6, S7, and Figure 2c, and the exhaustive parameters are illustrated in Table S2. The surface tensions (γ_s) of pure PM6 based on as-cast, TA- and CS_2-treatments were calculated at 26.59, 25.72 and 25.39 mN m^{-1}, respectively. The γ_s values of neat Y6 with as-cast, TA- and CS_2-processes were 27.8, 29.12, and 28.75 mN m^{-1}, respectively. For the PM6:Y6 blend films with as-cast, TA- and CS_2-processing, the calculated γ_s values were 27.29, 26.71, and 25.55 mN m^{-1}, respectively. Notably, the γ_s values of the blend films were between that of the pure donor and acceptor materials, and the γ_s value of the CS_2-treated blend film was near that of Y6, indicating more Y6 enriched on the surface of the blend film. However, the γ_s value with the untreated blend film was close to that of PM6, indicating more PM6 enriched on the surface of the blend film [41,42]. Based on these data, the vertical distribution of the donor and acceptor in blend film was altered with CS_2-treatment [43,44]. Therefore, the CS_2-treated blend film can improve the vertical transport of charge, resulting in the higher J_{SC} [42].

As shown in Figure 3, the morphologies of the as-cast, TA- and CS_2-treated blends were further investigated by atomic force microscopy (AFM) and transmission electron microscopy (TEM). Since the value roughness of CS_2-treated blend film (R_q=0.865 nm) was lower than those of TA

(R_q=0.907 nm) and as-cast (R_q=0.921 nm), the AFM height image indicated a smoother surface, resulting in improved J_{SC} and FF [45]. From the TEM images, the as-cast film demonstrates a well-mixed blend film morphology, indicating the enough donor/acceptor interface for charge transfer. For the TA-treated blend film, some aggregation occurred an even distribution of the acceptor. Compared with other processing methods, the CS_2-processed blend film shows a suitable area to form the interconnection network, which will facilitate exciton dissociation and charge transfer [46].

The photoluminescence (PL) spectra of neat film Y6 and its blend films with as-cast, TA-, and CS_2-treatments were measured with excitation at 550 nm, as illustrated in Figure 4a, b, to characterize the molecule interaction and research the dissociation of the photo-induced excitons of Y6 and charge transfer process from Y6 to PM6. The photoluminescence of the neat Y6 film without posttreatment presented a wide range of emission. After TA- and CS_2-treatments, the Y6 film showed red-shifted emission peak sequences from 962 nm to 968 and 978 nm, confirming the increasing molecular interaction induced by CS_2-annealing. When the polymer donor (PM6) and non-fullerene small molecule acceptor (Y6) were mixed together, the PL intensity of Y6 was largely quenched, suggesting that the excitons of Y6 can be beneficially dissociated in blends with as-cast, TA- and CS_2-treatments. Nevertheless, the maximum fluorescence intensity of the blend film of CS_2-treated PM6:Y6 was significantly lower than that of as-cast and TA-treated ones, indicating more efficient exciton dissociation [47].

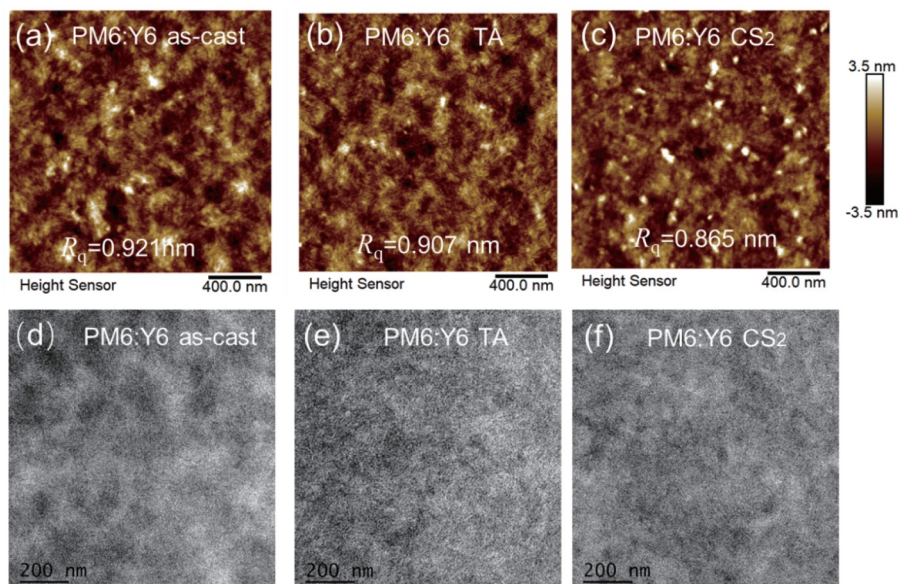To understand the evolution for photovoltaic performance,

Figure 3 The AFM height images (a–c) and the TEM images (d–f) of the blend films of PM6:Y6 with as-cast, TA- and CS$_2$-treatments, respectively (color online).

devices with different processing conditions were characterized *via* analyzing photocurrent density (J_{ph}) dependence on effective voltage (V_{eff}), as shown in Figure 4c and Table S3. We clearly found that the CS$_2$-treated device obtained the simultaneously maximum η_{diss} (98.56%) and η_{coll} (89.76%), presenting more efficient exciton dissociation and charge collection. This is consistent with the highest PCE (18.01%) of CS$_2$-treated devices [48]. The J_{ph} of CS$_2$-treated devices reached saturation faster than did that of the as-cast and TA-treated devices. The improved charge carrier transport and decreased charge recombination rate ensured a higher J_{SC} of 27.49 mA cm^{-2} and FF of 78.19% for CS$_2$-treated devices.

To elaborate the charge transport ability of three blend films, the carrier mobility was further measured by the space charge limited current (SCLC) method. As exhaustively depicted in Figure 4d, Figure S9 and Table S4, the hole mobilities (μ_h)/electron mobility (μ_e) of as-cast, TA- and CS$_2$-processing devices are 2.55×10^{-4}/2.72×10^{-4}, 2.99×10^{-4}/3.35×10^{-4}, and 4.08×10^{-4}/3.93×10^{-4} cm^2 V^{-1} s^{-1}. It is obvious that the values of μ_h and μ_e for the CS$_2$-treated devices are significantly higher than that of as-cast and TA-treated ones, thereby leading to the higher J_{SC}. Besides, the CS$_2$-treated device (μ_h/μ_e=1.03) has a more balanced carrier transport compared with as-cast (μ_h/μ_e=0.89) and TA-treated (μ_h/μ_e=0.91) devices, indicating a more effective charge transportation, thereby the higher FF. Consequently, the higher as well as better-balanced carrier mobilities of the CS$_2$-treated blend film results in an increased J_{SC} and FF.

To analyze the exciton generation and charge transfer in different processing blend films, we further performed transient absorption spectroscopy. As illustrated in Figure 4e,

f and Figure S10, we selectively excited NFA Y6 in three blend films at 800 nm pump pulse with delay time of 0.1–1,000 ps, and measured the transient absorption spectra. All the blend films exhibited bleach peaks at 632 and 803 nm, corresponding to the ground state bleach (GSB) of PM6 and Y6, respectively. At the same time, compared with the as-cast film, the GSB peaks of the TA- and CS$_2$-treated blend films decreased gradually and accompanying that, the GSB of PM6 rise relatively, implying hole transfer from Y6 to PM6. Figure 4f depicted the comparison of the early temporal kinetics at 825 nm. The decay time of as-cast (1.09 ps), TA- (0.99 ps) and CS$_2$- (0.95 ps) treatment blend films decreased sequentially. As a result, the fastest electron transfer in the PM6:Y6 films with CS$_2$-annealing formed the better photovoltaic performance, covering from J_{SC} to PCE [48,49].

The AM 1.5G solar spectrum is composed of ultraviolet, visible, and near-infrared regions [50]. The energy distribution of sunlight is the largest, covering 51% of the NIR region, while the visible spectrum and UV spectrum cover 47% and 2%, respectively. The response curve of the human eye is narrowly distributed in the visible spectrum of 370–780 nm. After we found that solvent annealing could broaden its absorption range in the visible and near-infrared regions, a semitransparent organic solar cell based on CS$_2$-treated PM6:Y6 blend film was fabricated. It was covered with 1 nm ultra-thin Cu and Ag of different thicknesses (5, 10, and 15 nm) and employed as the top electrode. The *J-V* curves of semitransparent OSCs were measured under simulated AM 1.5G solar illumination, as shown in Figure 5a, and the related photovoltaic results are elaborated in Table 2. It could be apparent that J_{SC} values of semitransparent OSCs
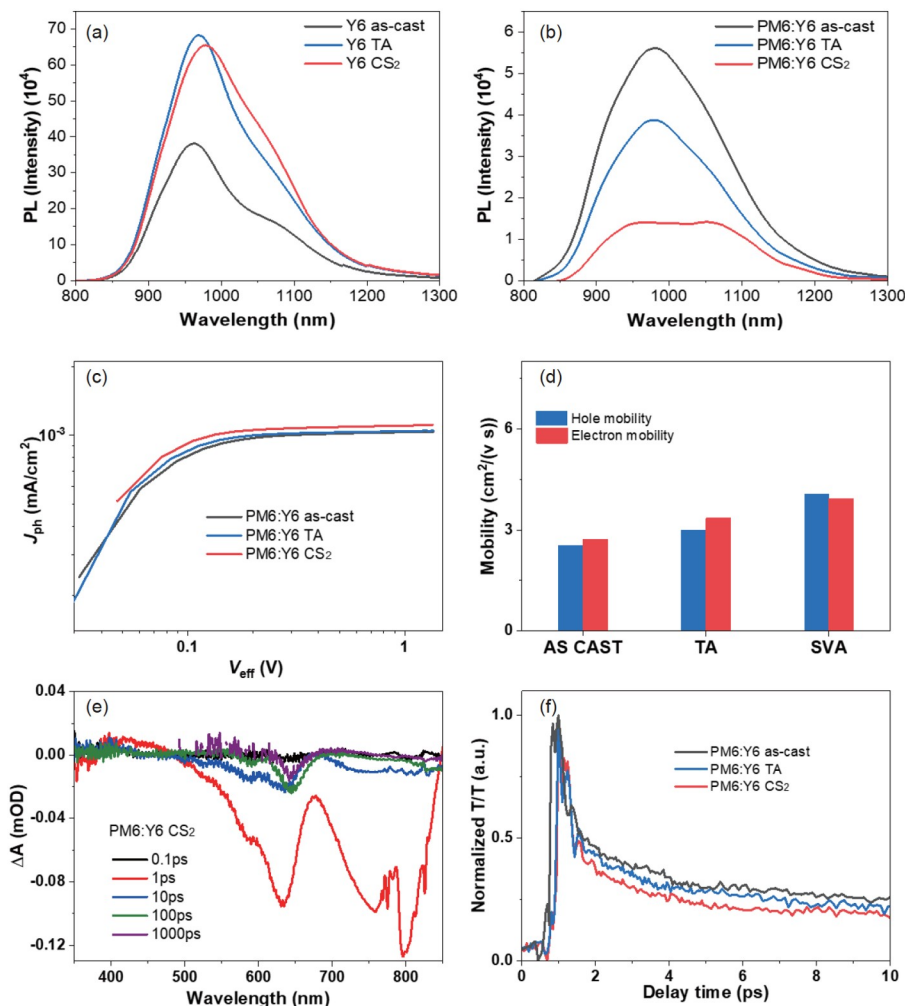
Figure 4 (a) Photoluminescence spectra of pristine Y6 film with various treatments; (b) photoluminescence spectra of the blend PM6:Y6 film under different processing; (c) J_{ph}-V_{eff} curves of devices containing different treatments; (d) the electron and hole mobilities of PM6:Y6 with different treatments; (e) spectra of CS_2-treated PM6:Y6 blend films at a certain delay time; (f) transient absorption time dynamics of PM6:Y6 blend films based on various treatments (color online).

are increased along with the increase of Ag thickness, and the results ascribed to decreased photon loss from the electrode [51]. With further increase in Ag thickness, FF could be gradually increased, mainly owing to the increased conductivity of the electrode [52]. By replacing the thickness of Ag layer as 10, 15, and 20 nm, the PCE and AVT values of semitransparent OSCs with the optimized result were 11.41% and 20.45%, 13.07% and 19.33%, 13.99% and 17.45%, respectively. Figure 5b shows the external quantum efficiency (EQE) spectra of semitransparent OSCs among optimal processing, and the difference between the measured and calculated J_{SC} of the translucent OSC is less than 6%. The transmittance spectrum of the semitransparent OSC was characterized, as shown in Figure 5c. We found that the average visible-light transmittance (AVT) values of the semitransparent OSCs gradually decreased with increasing Ag layer thickness. The PCE and AVT of semitransparent

OSCs can be balanced *via* changing electrode thickness. Light utilization efficiency (LUE), utilized to evaluate the devices' overall performance, is defined as the product of PCE and AVT in semitransparent OSCs. With Cu (1 nm) and Ag (15 nm) as electrodes, the PCE and AVT of semitransparent OSCs were obtained at 13.07% and 19.33% in the optimized process, which is one of the highest LUE (2.53%) values for PM6:Y6 binary semitransparent OSCs.

To evaluate human visual color perception, the color features of semitransparent OSCs were analyzed *via* the Commission Internationale d'Eclairage (CIE) 1931xyY chromaticity diagram [1,53]. As presented in Figure 5d, the color coordinates (*x*, *y*) for LPOSCs based on optimized results are (0.2382, 0.2323), (0.2411, 0.2391), and (0.2461, 0.2462) for 20, 15, and 10 nm of the Ag electrode, respectively. There is not only a clear pattern of the school emblem through the ST-OSCs (as illustrated in Figure S11), but also a
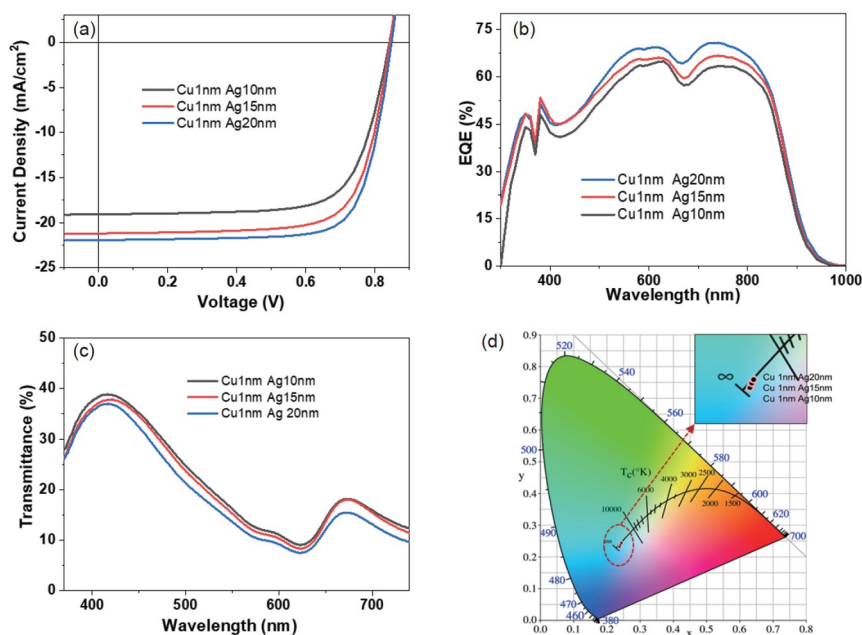
Figure 5   (a) *J-V* curves for semitransparent devices with CS_2-treatment; (b) corresponding EQE curves for semitransparent devices under CS_2 treatment; (c) transmission spectra; (d) color coordinates of semitransparent CS_2-treated OSCs on the CIE chromaticity diagram (color online).

Table 2   Photovoltaic performance of semitransparent based on PM6:Y6 active layer

Ag thickness (nm)	V_{OC} (V)	J_{SC} (mA cm^{-2})	$J_{calc.}$ [a] (mA cm^{-2})	FF (%)	PCE (Ave.±Dev.) [b] (%)	AVT [c]	LUE (%)
10	0.841	19.07	18.71	71.19	11.41 (11.24±0.11)	20.45	2.33
15	0.842	21.19	19.98	73.27	13.07 (12.93±0.09)	19.33	2.53
20	0.845	21.95	20.62	75.45	13.99 (13.81±0.10)	17.45	2.44

a) The J_{SC} of semitransparent CS_2-treated OSCs were obtained from EQE spectrum; b) average and deviation of 15 samples of semitransparent devices; c) AVT (370–740 nm) [54,55].

remarkable transmission in visible light range, indicating that our ST-OSCs have practical applications.

3   Conclusions

In conclusion, OSCs treated with different processing were fabricated based on PM6:Y6 blend films and their device efficiencies were measured. A remarkable PCE of 18.01% with a V_{OC} of 0.839 V, a J_{SC} of 27.45 mA cm^{-2} and an FF of 78.19% for CS_2-treated devices was obtained. Based on the most optimized process, employing Cu (1 nm) and Ag (15 nm) as the cathode to fabricate semitransparent OSCs can achieve a remarkable PCE of 13.07% with a corresponding 19.33% AVT, arriving at the largest LUE (2.53%). It was found that the morphology of the active layer was optimized by this solvent annealing method, showing increased molecular crystallinity and improved vertical charge transport performance. In addition, the relationship between film morphology and device performance with various treatments has been systematically studied. Our work reveals a simple but effective SVA process to optimize active layer film morphology for enhanced photovoltaic performance.

Conflict of interest   The authors declare no conflict of interest.

Supporting information   The supporting information is available online at http://chem.scichina.com and http://link.springer.com/journal/11426. The supporting materials are published as submitted, without typesetting or editing. The responsibility for scientific accuracy and content remains entirely with the authors.

1   Colsmann A, Puetz A, Bauer A, Hanisch J, Ahlswede E, Lemmer U. *Adv Energy Mater*, 2011, 1: 599–603

2   Tuladhar SM, Azzouzi M, Delval F, Yao J, Guilbert AAY, Kirchartz T, Montcada NF, Dominguez R, Langa F, Palomares E, Nelson J. *ACS Energy Lett*, 2016, 1: 302–308

3   Xue P, Cheng P, Han RPS, Zhan X. *Mater Horiz*, 2022, 9: 194–219

4   Sun L, Zeng W, Xie C, Hu L, Dong X, Qin F, Wang W, Liu T, Jiang X, Jiang Y, Zhou Y. *Adv Mater*, 2020, 32: 1907840

5   Dong X, Shi P, Sun L, Li J, Qin F, Xiong S, Liu T, Jiang X, Zhou Y. *J Mater Chem A*, 2019, 7: 1989–1995

6   Kaltenbrunner M, Sekitani T, Reeder J, Yokota T, Kuribara K, Tokuhara T, Drack M, Schwödiauer R, Graz I, Bauer-Gogonea S, Bauer S, Someya T. *Nature*, 2013, 499: 458–463

7   Cui Y, Xu Y, Yao H, Bi P, Hong L, Zhang J, Zu Y, Zhang T, Qin J, Ren J, Chen Z, He C, Hao X, Wei Z, Hou J. *Adv Mater*, 2021, 33: 2102420

8   Chong K, Xu X, Meng H, Xue J, Yu L, Ma W, Peng Q. *Adv Mater*, 2022, 34: 2109516

9   Liu Y, Liu B, Ma CQ, Huang F, Feng G, Chen H, Hou J, Yan L, Wei Q, Luo Q, Bao Q, Ma W, Liu W, Li W, Wan X, Hu X, Han Y, Li Y, Zhou Y, Zou Y, Chen Y, Li Y, Chen Y, Tang Z, Hu Z, Zhang ZG, Bo Z. *Sci China Chem*, 2022, 65: 224–268

10 Xie L, Zhang J, Song W, Hong L, Ge J, Wen P, Tang B, Wu T, Zhang X, Li Y, Ge Z. *ACS Appl Mater Interfaces*, 2021, 13: 20405–20416

11 Cui C, Li Y. *Aggregate*, 2021, 2: e31

12 Datt R, Suman R, Bagui A, Siddiqui A, Sharma R, Gupta V, Yoo S, Kumar S, Singh SP. *Sci Rep*, 2019, 9: 8529

13 Zhao F, Wang C, Zhan X. *Adv Energy Mater*, 2018, 8: 1703147

14 Zhang H, Li Y, Zhang X, Zhang Y, Zhou H. *Mater Chem Front*, 2020, 4: 2863–2880

15 Garcia Romero D, Di Mario L, Portale G, Loi MA. *J Mater Chem A*, 2021, 9: 23783–23792

16 Ge J, Hong L, Song W, Xie L, Zhang J, Chen Z, Yu K, Peng R, Zhang X, Ge Z. *Adv Energy Mater*, 2021, 11: 2100800

17 Guo X, Fan Q, Wu J, Li G, Peng Z, Su W, Lin J, Hou L, Qin Y, Ade H, Ye L, Zhang M, Li Y. *Angew Chem Int Ed*, 2021, 60: 2322–2329

18 Zhu L, Zhang M, Zhou G, Hao T, Xu J, Wang J, Qiu C, Prine N, Ali J, Feng W, Gu X, Ma Z, Tang Z, Zhu H, Ying L, Zhang Y, Liu F. *Adv Energy Mater*, 2020, 10: 1904234

19 Li Y, Zheng N, Yu L, Wen S, Gao C, Sun M, Yang R. *Adv Mater*, 2019, 31: 1807832

20 Chen D, Nakahara A, Wei D, Nordlund D, Russell TP. *Nano Lett*, 2011, 11: 561–567

21 Xiao L, Yan C, Li Z, Zhong W, Tan W, Liu Y, Liu F, Peng X, Min Y. *ACS Appl Energy Mater*, 2021, 4: 4234–4241

22 Verploegen E, Miller CE, Schmidt K, Bao Z, Toney MF. *Chem Mater*, 2012, 24: 3923–3931

23 Wang Z, Peng Z, Xiao Z, Seyitliyev D, Gundogdu K, Ding L, Ade H. *Adv Mater*, 2020, 32: 2005386

24 Li G, Shrotriya V, Huang J, Yao Y, Moriarty T, Emery K, Yang Y. *Nat Mater*, 2005, 4: 864–868

25 Li G, Shrotriya V, Yao Y, Yang Y. *J Appl Phys*, 2005, 98: 043704

26 Xie Y, Zhou W, Yin J, Hu X, Zhang L, Meng X, Ai Q, Chen Y. *J Mater Chem A*, 2016, 4: 6158–6166

27 Xiao L, Li Z, Hu Q, Liu Y, Zhong W, Mei X, Russell TP, Liu Y, Min Y, Peng X, Cao Y. *J Mater Chem C*, 2019, 7: 9618–9624

28 Wang JL, Xiao F, Yan J, Wu Z, Liu KK, Chang ZF, Zhang RB, Chen H, Wu HB, Cao Y. *Adv Funct Mater*, 2016, 26: 1803–1812

29 Wang JL, Liu KK, Yan J, Wu Z, Liu F, Xiao F, Chang ZF, Wu HB, Cao Y, Russell TP. *J Am Chem Soc*, 2016, 138: 7687–7697

30 Zhu C, Huang H, Jia Z, Cai F, Li J, Yuan J, Meng L, Peng H, Zhang Z, Zou Y, Li Y. *Sol Energy*, 2020, 204: 660–666

31 Zheng L, Li M, Dai S, Wu Y, Cai Y, Zhu X, Ma S, Yun D, Li JF. *J Phys Chem C*, 2021, 125: 18623–18629

32 Xie Y, Huo L, Fan B, Fu H, Cai Y, Zhang L, Li Z, Wang Y, Ma W, Chen Y, Sun Y. *Adv Funct Mater*, 2018, 28: 1800627

33 Yuan J, Zhang Y, Zhou L, Zhang G, Yip HL, Lau TK, Lu X, Zhu C, Peng H, Johnson PA, Leclerc M, Cao Y, Ulanski J, Li Y, Zou Y. *Joule*, 2019, 3: 1140–1151

34 Yao J, Qiu B, Zhang ZG, Xue L, Wang R, Zhang C, Chen S, Zhou Q, Sun C, Yang C, Xiao M, Meng L, Li Y. *Nat Commun*, 2020, 11: 2726

35 Li X, Ma R, Liu T, Xiao Y, Chai G, Lu X, Yan H, Li Y. *Sci China Chem*, 2020, 63: 1256–1261

36 Li K, Wu Y, Li X, Fu H, Zhan C. *Sci China Chem*, 2020, 63: 490–496

37 Wu Y, Zheng Y, Yang H, Sun C, Dong Y, Cui C, Yan H, Li Y. *Sci China Chem*, 2020, 63: 265–271

38 Jung FA, Berezkin AV, Tejsner TB, Posselt D, Smilgies DM, Papadakis CM. *Macromol Rapid Commun*, 2020, 41: 2000150

39 Zhan L, Li S, Lau TK, Cui Y, Lu X, Shi M, Li CZ, Li H, Hou J, Chen H. *Energy Environ Sci*, 2020, 13: 635–645

40 Ma X, Wang J, Gao J, Hu Z, Xu C, Zhang X, Zhang F. *Adv Energy Mater*, 2020, 10: 2001404

41 Yu R, Wu G, Cui Y, Wei X, Hong L, Zhang T, Zou C, Hu S, Hou J, Tan Z. *Small*, 2021, 17: 2103497

42 Hong L, Yao H, Cui Y, Bi P, Zhang T, Cheng Y, Zu Y, Qin J, Yu R, Ge Z, Hou J. *Adv Mater*, 2021, 33: 2103091

43 Zhang L, Yi N, Zhou W, Yu Z, Liu F, Chen Y. *Adv Sci*, 2019, 6: 1900565

44 Li J, Wang Y, Liang Z, Wang N, Tong J, Yang C, Bao X, Xia Y. *ACS Appl Mater Interfaces*, 2019, 11: 7022–7029

45 Hong L, Yao H, Cui Y, Yu R, Lin YW, Chen TW, Xu Y, Qin J, Hsu CS, Ge Z, Hou J. *Small*, 2021, 17: 2101133

46 Wang H, Zhang Z, Yu J, Lin PC, Chueh CC, Liu X, Guang S, Qu S, Tang W. *ACS Appl Mater Interfaces*, 2020, 12: 21633–21640

47 Gao X, Yu K, Zhao Y, Zhang T, Wen J, Liu Z, Liu Z, Ye G, Gao J, Ge Z, Liu Z. Chin Chem Lett, 2021, doi: 10.1016/j.cclet.2021.12.055

48 Zhang M, Zhu L, Zhou G, Hao T, Qiu C, Zhao Z, Hu Q, Larson BW, Zhu H, Ma Z, Tang Z, Feng W, Zhang Y, Russell TP, Liu F. *Nat Commun*, 2021, 12: 309

49 Chen Z, Song W, Yu K, Ge J, Zhang J, Xie L, Peng R, Ge Z. *Joule*, 2021, 5: 2395–2407

50 Huang X, Oh J, Cheng Y, Huang B, Ding S, He Q, Wu FY, Yang C, Chen L, Chen Y. *J Mater Chem A*, 2021, 9: 5711–5719

51 Hu Z, Wang Z, Zhang F. *J Mater Chem A*, 2019, 7: 7025–7032

52 Ma X, Xiao Z, An Q, Zhang M, Hu Z, Wang J, Ding L, Zhang F. *J Mater Chem A*, 2018, 6: 21485–21492

53 Li Y, Lin JD, Che X, Qu Y, Liu F, Liao LS, Forrest SR. *J Am Chem Soc*, 2017, 139: 17114–17119

54 Xu C, Jin K, Xiao Z, Zhao Z, Ma X, Wang X, Li J, Xu W, Zhang S, Ding L, Zhang F. *Adv Funct Mater*, 2021, 31: 2107934

55 Hu Z, Wang J, Ma X, Gao J, Xu C, Wang X, Zhang X, Wang Z, Zhang F. *J Mater Chem A*, 2021, 9: 6797–6804